For Earth and Planetary Science Letters

Mesoarchean diamonds formed in thickened lithosphere, caused by slab-stacking

S Timmerman<sup>1\*</sup>, JR Reimink<sup>2</sup>, A Vezinet<sup>1</sup>, F Nestola<sup>3</sup>, K Kublik<sup>1</sup>, A Banas<sup>1</sup>, T Stachel<sup>1</sup>,

RA Stern<sup>1</sup>, Y Luo<sup>1</sup>, C Sarkar<sup>1</sup>, A lelpi<sup>4</sup>, CA Currie<sup>1</sup>, C Mircea<sup>5</sup>, V Jackson<sup>6</sup>, DG Pearson<sup>1</sup>

<sup>1</sup> University of Alberta, Canada

\*corresponding author: suzette@ualberta.ca

<sup>2</sup> Pennsylvania State University, US

<sup>3</sup> University of Padua, Italy

<sup>4</sup> Laurentian University, Canada

<sup>5</sup> Saskatchewan Research Council, Canada

<sup>6</sup> Northwest Territories Geological Survey, Canada (*retired*)

**Abstract** 

When and how Earth's ancient crust – the cratons - became underpinned by cool, thick

lithospheric mantle roots capable of hosting diamonds are among the most controversial

aspects of Archean geology. Alluvial diamonds in cratonic sedimentary cover rocks,

whose minimum age is determined by detrital-zircon geochronology, provide a unique

perspective on this topic. A new discovery of a diamond-bearing quartz-pebble

conglomerate from the northern Slave craton, Canada contains detrital zircon with a

1

restricted U-Pb age distribution that has a dominant peak at ~2.94 Ga and depositional age of ~2.83 Ga. Pressure-temperature constraints derived from an olivine-diamond host pair lie on a conductive Mesoarchean geotherm of ~36–38 mW/m², comparable to the coolest modern lithospheric geotherms. This result is at odds with a hotter geothermal gradient related to nearby Mesoarchean komatiites. We propose a model whereby early building blocks for cratons were small but with deep cool roots that formed by slabstacking, and were subsequently juxtaposed with regions of thinner, hotter lithosphere. This heterogeneous initial architecture later amalgamated and thickened through lateral accretion forming the more uniformly thick cratonic lithosphere observed today. Thermal modelling indicates that stacking/thickening of cool initial lithosphere into a lithospheric keel thick enough to stabilise diamonds is the most likely way of generating the observed geotherm by Mesoarchean times.

Keywords: diamond, geotherm, Mesoarchean, lithosphere formation, zircon, craton

#### 1. Introduction

Constraining the state of cratonic lithospheric geotherms in the early Earth is critical to understanding the building blocks of cratons and their potential mineral endowments. Global compilations of mantle lithosphere ages show major peaks in lithosphere formation since ~3.0 Ga (Pearson et al. 2021), although lithosphere cool enough to host diamonds was present earlier (e.g., Westerlund et al. 2006; Smart et al. 2016). Therefore, the likely existence of lithosphere thick and cool enough to form Meso- to even Palaeoarchean diamonds raises many questions about the lithospheric architecture in early cratons,

especially given the broadly coeval presence of abundant ultramafic magmatism on and around early cratons (Arndt et al. 2008), perhaps indicative of thin, hot lithosphere.

Whereas many diamonds have ancient formation ages (up to 3.5 Ga; Smit et al. in press), most available for study were extracted from the mantle, by kimberlite eruption, in the last 1.1 Gyr, and hence any unambiguous information provided by their inclusions about lithospheric geotherms relates to more recent history. In contrast, diamonds extracted from Earth's mantle during the early stages of craton evolution provide a clear window into the thermal state of the Archean lithosphere. Such diamonds are very scarce, being reported only from Meso- to Neoarchean Witwatersrand sediments of South Africa (Raal 1962; Smart et al. 2016) and Neoarchean lamprophyres/volcaniclastic sediments from Wawa, Ontario, Canada (e.g. Stachel et al. 2006).

Here, we describe a new discovery of diamond-bearing Mesoarchean meta-sedimentary supracrustal rocks (hereafter termed 'sediments' for the sake of simplicity) in the northern Slave craton. We use U-Pb ages of detrital zircons from these sediments to evaluate qualitative aspects of catchment size and their maximum depositional age. The microdiamonds preserved in these sediments are described and we present C and N isotope data from these diamonds, as well as inclusion barometry from one of the diamonds containing an olivine inclusion. We discuss the implications of these data in the context of the broader Slave craton paleogeography and geology in the Mesoarchean, and propose a testable model to explain lithospheric root formation in this region.

# 2. Geological background and samples

Gold-bearing quartz-pebble conglomeratic strata – likely deposited by alluvial fans or coarse-grained rivers – are 15-20 m thick and are found in the stratigraphically lower portions of the Slave craton cover-group sequence within the Tree River area of the northern Slave craton, Nunavut, Canada (Jackson 1997; Figure 1). The basal conglomerate non-conformably overlies the Central Slave Basement complex consisting of granite-tonalite gneiss. Quartzite clasts from the conglomerate are mineralogically very mature, with clast sizes from a few mm to 3 cm. Cross-bedded sandstone conformably overlies the conglomerate.

Three detrital microdiamonds (<220 µm) with octahedral morphologies modified by minor cuboid faces (Figure 2) were recovered from ~15 kg of this basal conglomerate, processed for high-yield diamond separation at the Saskatchewan Research Council, Canada. From the same processed conglomerate sample some zircon grains were simultaneously extracted. The majority – several hundred more zircon grains – were obtained from a separate sample collected from the conformably and directly overlying cross-bedded sandstone.

#### 3. Methods

Details of Sm-Nd isotope analyses using Neptune MC-ICPMS and C-N isotope analyses using SIMS are provided in the supplementary information, and here we summarize the zircon and diamond methods.

## 3.1 Sample preparation

A 15 kg conglomerate sample for diamond recovery was processed by the SRC using their accredited micro-diamond recovery process. Both zircon grains and diamonds were recovered. More zircon grains were liberated from the overlying sandstone using SELFRAG electronic pulse disaggregation technology at the University of Alberta. Fragmented material was dried, sieved and crystals < 330 µm were separated by differential gravity using a regular flat-bottom gold pan. Collectively, a total of > 600 zircon crystals were mounted and imaged via scanning electron microscopy (SEM) utilizing a Zeiss EVO MA15 instrument equipped with a high-sensitivity, broadband cathodoluminescence (CL) and backscattered electron (BSE) detectors. Beam conditions were 15 – 20 kV and 3 – 5 nA sample current.

The diamonds were analysed by XRD and FTIR unpolished, followed by individual mounting in epoxy and polishing with metal-bonded diamond grinding disks to approximately one-third depth. The diamond epoxy mounts were cut into smaller epoxy blocks and mounted together with SIMS standards and coated with 25 nm of Au for CL imaging. CL imaging was performed using a Zeiss EVO MA15 scanning electron microscope instrument at the Canadian Centre for Isotopic Microanalysis at the University of Alberta. Images were taken with a parabolic mirror coupled to a high-sensitivity,

broadband photomultiplier detector and using an operating voltage of 15 kV and beam current of 3 – 5 nA.

## 3.2 U-Pb isotope analyses

Uranium and lead analyses of zircon grains were carried out on the sector-field LA-ICP-MS at the Canadian Facility for Isotopic and Geochemical Research, University of Alberta. U-Pb and Hf analyses were conducted in laser split-stream mode on the same spots; Hf isotope results will be published elsewhere. Zircons were ablated with a 33 or 44 um spot size for 45 seconds with a repetition rate of 8 Hz, using a 193 nm laser (Resolution ArF excimer). A Thermo Fisher Scientific Element2 XR instrument was used to measure masses <sup>202</sup>Pb, <sup>208</sup>Pb, <sup>232</sup>Th (measured in triple mode), <sup>206</sup>Pb and <sup>238</sup>U (measured in analogue mode) and <sup>204</sup>Pb plus <sup>207</sup>Pb (measured in counting mode). Standard zircon LH94-15 was used as primary reference material, Plesovice, GJ-1, 91500 and FC-1 zircons were used as secondary standards (see details in supplementary information). Data was reduced with the lolite software and all results are provided in Supplementary Table S1, images are shown in Figure S3. More analytical details are summarised in the table (Table 1) below, in the supplementary information, and in Vezinet et al. (2020). U-Pb data that are not near-concordant (meaning not within 5% of the concordia curve) are affected by Pb loss and are not used in the interpretation but are provided in the supplementary data for completeness (Table S1).

Table 1: overview of settings for U-Pb analyses.

Laboratory & Sample Preparation							
Laboratory name Sample type/mineral Sample preparation Imaging	Arctic Resource Lab, University of Alberta (Canada)  Zircon grains  Conventional mineral separation, polished 1 inch resin mount,  CL & BSE (Gemini supra 55 VP Zeiss; EVO MA15 Zeiss; JEOL JSM-5910 LV)  Laser ablation system						
	-						
Make, Model & type Ablation cell Laser wavelength Pulse width	RESOlution ArF excimer  Laurin Technic S-155  193 nm  20 ns						
Fluence Repetition rate	6J cm <sup>-2</sup> 8 Hz						
Ablation/Washout duration	45 secs / 60 secs						
Ablation rate	0.125µm.pulse <sup>-1</sup>						
Spot diameter nominal/actual	33 µm / 44 µm						
Sampling mode / pattern Carrier gas	Static spot ablation 100% He in the cell, 0.8 l.min <sup>-1</sup>						
	ICP-MS Instrument						
	U-Th-Pb measurements						
Make, Model & type Sample introduction RF power	Thermo Fisher Scientific, Element XR, SC-SF-ICP-MS Ablation aerosol introduced through Tygon tubing 1360W						
Make-up gas flow (I/min)	Total gas is made of ∼1.6 l.min⁻¹ of Ar, 0.8 l.min⁻¹ of He and 12-14 ml.min⁻¹ of №. This total gas is divided between both ICP-MS at a ~ 50-50 rate.						
Detection system	202, 208, 232 in triple mode.						
Masses measured	202, 204, 206, 207, 208, 232, 238						
Integration time per peak/ dwell times	30 ms on 202, 204, 208 and 232; 60 ms on 206, 207 and 238						
Total integration time IC Dead time	300 ms for each output datapoint						
io Boda iiiio	Data Processing						
Gas blank	40 second on-peak zero subtracted for U-Pb measurements						
Calibration strategy	LH94-15 used as primary reference material, Plešovice, GJ-1, 91500 & FC-1 used as secondaries/validation materials.						
Reference Material info	LH94-15 Plešovice FC-1						
Data processing package used / Correction for LIEF	Iolite software package using the following DRS: "U_Pb Geochron 4" for U-Th-Pb isotope analyses. LIEF correction assumes matrix match between reference material and samples.						
Mass discrimination	Standard-sample bracketing with <sup>207</sup> Pb/ <sup>206</sup> Pb and <sup>206</sup> Pb/ <sup>238</sup> U normalized to primary reference material.						
Common-Pb correction, composition and uncertainty	No common-Pb correction applied to the data						
Uncertainty level & propagation	Ages are quoted at a coverage factor of 2, absolute. Propagation is by quadratic addition. Reproducibility and age uncertainty of reference material and common-Pb composition uncertainty are propagated where appropriate.						
Quality control / Validation	Results of U-Pb analyses on validation zircon reference material are reported in Supplementary data table.						

# 3.3 Fourier transform infrared spectroscopy (FTIR) and Secondary Ion Mass Spectrometry (SIMS)

Diamond spectra (resolution of 4 cm<sup>-1</sup>, range 4000-650 cm<sup>-1</sup>, 200 scans in transmission mode using a 100  $\mu$ m square aperture) were obtained with a Thermo Nicolet Nexus 470 FT-IR Spectrometer, coupled to a continuum infrared microscope with a liquid nitrogen cooled detector, at the University of Alberta. Each spectrum is background corrected, baselined, and normalized to 1 cm diamond thickness. The nitrogen peak area was deconvoluted into the A, B, and D components using the CAXBD spreadsheet written by David Fisher (De Beers) and converted into nitrogen concentrations using the absorption strength at 1282 cm<sup>-1</sup> for A-centres (16.5  $\pm$  0.1) and B-centres (79.4  $\pm$  0.8). Details of absorption coefficients are given in Cartigny et al. (2009).

Mounts were coated with 100 nm Au film prior to SIMS analyses. The N abundances, C-isotopes (<sup>13</sup>C/<sup>12</sup>C), and N-isotopes (<sup>15</sup>N/<sup>14</sup>N) were determined by SIMS analyses with a Cameca IMS-1280 multi-collector ion microprobe at the Canadian Facility for Isotopic and Geochemical Research, University of Alberta, using methods and the diamond S0270 / vitreous carbon S0233A reference materials described in detail in the supplementary information, using established procedures at CCIM at the University of Alberta (Stern et al., 2014).

## 3.4 Single crystal X-ray diffraction

Single-crystal X-ray diffraction measurements were performed on the TR-18-02-d2 diamond, which shows a clear octahedral morphology. The diamond was investigated using a Rigaku-Oxford Diffraction Supernova diffractometer equipped with a 200K Pilatus Dectris detector and an X-ray microsource (Mo Kα wavelength) at the Department of Geosciences, University of Padova. The X-ray beam was 120 µm in diameter and the sample-to-detector distance was 68 mm. The longest dimension of the diamond was about 212 µm and it contained no optically visible inclusions. However, in order to detect possible invisible mineral inclusions, a very long X-ray data collection was carried out scanning the entire diamond; we collected 985 frames over 15 different runs up to 20 max = 60° (full Ewald sphere) with an exposure time of 140 seconds per frame and a total data collection time of ~38 hours. Beyond the typical and expected diffraction reflections from the diamond crystal, we identified diffraction reflections from an inclusion of olivine. Based on the intensity of the main olivine reflections (see Supplementary Figure S1 for the 112 olivine reflection) with respect to the main diffraction peak of the diamond host, we can estimate an olivine crystal size of ≤20 µm (based on observations of hundreds of olivine inclusions still trapped in diamonds studied using the same instrumentation).

Olivine is an ideal solid solution between forsterite (Fo) and fayalite (Fa) and its unit-cell volume linearly changes as a function of the forsterite component, where a higher Fo component results in a unit-cell volume decrease. The volume change as a function of the Fo-Fa content can be expressed by the linear relationship (Nestola et al. 2011):

 $V (Å^3) = 308.56 - 0.1801 \times \% Fo$ 

With the measured unit-cell volume and an assumed %Fo, the pressure on the inclusion (P<sub>inc</sub>) can be calculated with the pressure-volume equation of state of olivine published by Angel et al. (2017). With the P<sub>inc</sub> and the equations of states for olivine (Angel et al. 2017) and diamond (Angel et al. 2015), we can use the software EoSFitPinc (Angel et al. 2017) to provide the pressure (or depth) of formation, P<sub>trap</sub>.

## 3.5 Thermal modelling of lithosphere evolution

We calculated 1D time-dependent geotherms to evaluate the time frame over which a cold (slab) and hot (plume) initial thermal state model will cool/heat to yield conditions equivalent to those recorded by elastic thermobarometry of the olivine-diamond pair. The models started with an initial 1D thermal structure, and the thermal evolution was calculated using the conservative finite difference method (Gerya 2019) and assuming all heat is transferred conductively. For the cold initial state model, we assumed two stacked plates where each plate had an initial geotherm consistent with its thickness. The upper plate consists of 20 km upper crust, 20 km lower crust and 79 km lithospheric mantle, and the lower plate is oceanic lithosphere (also 119 km thick), resulting in a total thickness of 238 km. For the hot initial state scenario, we assumed a conductive geotherm that intersects a 1420 °C mantle adiabat at the Moho. Below the Moho, the temperature was raised by 150 °C above the adiabat to represent elevated temperatures associated with a mantle plume. The thermal evolution of each system was calculated for 2000 Myr, with a fixed temperature of 0 °C at the surface and the adiabatic temperature at 300 km depth, based on the mantle potential temperature and adiabatic gradient. Secular cooling was included by linearly decreasing the potential temperature. Below 238 km, a high thermal

conductivity was used as a proxy for mantle convection below the lithosphere. Model parameters are given in Table 2, where the radiogenic heat production and mantle secular cooling rate are taken from Eaton and Perry (2013). Each model approached a steady-state geotherm with a 238 km thick lithosphere. The same material properties were used for the steady-state geotherm reference model and approximates the steady-state "relaxed" geotherm of Hasterok and Chapman (2011; used as reference lines in Figure 5).

Table 2: Parameters used in geotherm calculations.

General Layer parameters	Thickness (km)	Thermal Conductivity (W m <sup>-1</sup> K <sup>-1</sup> )	Density (kg/m³)	Specific heat capacity (J kg <sup>-1</sup> K <sup>-1</sup> )
Upper Crust	20	2.25	2700	800
Lower Crust	20	2.25	2700	800
Mantle Lithosphere + cold slab	79 + 119 = 198	2.25	3300	800
Mantle Lithosphere (plume/relaxed geotherm)	198	2.25	3300	800
Asthenosphere	62	45	3300	800
Model specific parameters	Initial Surface	Radiogenic hea	nt production (μW/m³)	
most opening parameters	heat flow	radiogoo	it production (μπ////////////////////////////////////	
			lower crust,	
	(mW/m <sup>2</sup> )	upper crust	lithosphere*	asthenosphere
Cold Slab	47	1	0.0139	0
Hot Plume	96	1	0.0139	0
Steady-state Geotherm	20.95	0.36**	0.005**	0
Other parameters				
Tp (at t=0 Myr) (°C)	1420			
Tp (at t=2000 Myr) (°C)	1360			
Adiabatic gradient (°C km <sup>-1</sup> )	0.4			
Decay rate ( $\lambda$ ) (year <sup>1</sup> )***	5.10E-10			
Secular cooling rate of Tp (K Gyr <sup>-1</sup> )	-40			

<sup>\*</sup>Lower crust and lithosphere have the same radiogenic heat production values (Eaton and Perry, 2013)

#### 4. Results and Discussion

## 4.1 Mesoarchean conglomerate age and a small source catchment

<sup>\*\*</sup>Expected radiogenic heat production after 2000 Myr, following decay at rate  $\lambda$ .

<sup>\*\*\*</sup>Rate of decay for all radioactive materials.

We present the results from 199 detrital zircon grains, with dull internal micro-structures and abundant fractures (see Methods; 220 spot analyses on 199 crystals). U-Pb data that are not near-concordant encompass 40% of the analyses and are not used in the interpretation but are provided in the supplementary data for completeness (Table S1). High-quality U-Pb data within our concordance filter (n=131) are shown in Figure 3. The youngest concordant zircon has a <sup>207</sup>Pb/<sup>206</sup>Pb age of 2823 Ma ± 19 Ma. The bulk of concordant zircon U-Pb analyses have <sup>207</sup>Pb/<sup>206</sup>Pb ages between 2.9 Ga and 3.0 Ga (72%). A regression of the discordant grains with the youngest <sup>207</sup>Pb/<sup>206</sup>Pb ages yields a lower intercept age of ~1.2 Ga. Zircon grains with the youngest <sup>207</sup>Pb/<sup>206</sup>Pb ages may have experienced ancient Pb-loss. Therefore, the concordant grains with the youngest <sup>207</sup>Pb/<sup>206</sup>Pb ages, below 2.9 Ga, may record this Pb loss, making the maximum depositional age estimate based on the youngest concordant grain too young. We conclude that the maximum depositional age for this sediment is conservatively ~2.9 Ga, but may be slightly younger (2.83 Ga).

Older zircon cores have crystallization ages up to ~3.5 Ga, consistent with the oldest ages of the Slave craton basement complex outside of the Acasta Gneiss area (Reimink et al. 2019). Although the detrital zircons represent a felsic eroded component and the detrital diamonds are ultimately sourced from an eroded mafic volcanic rock, the maximum depositional age of the host rock is assumed to be the minimum age for all components, including the diamonds, and thus a minimum age for the geotherm constraints, discussed in section 4.3.

Although whole rock Nd isotopes of the Tree River conglomerate (Supplementary Table S2) yield depleted mantle model ages that range from ~3.0 Ga – the time of sediment deposition – to early Mesoarchean (3.5 Ga) and confirm the U-Pb age range from the zircons, it is more likely that the variation in Nd isotope composition (initial ε<sup>143</sup>Nd values = +0.4 to -5.0) at the time of sediment deposition (>2.83 Ga) indicates variation in the source sediment region. The distribution of detrital zircon ages provides valuable information on the tectonic setting at time of sediment deposition (Cawood et al. 2013; Reimink et al. 2021). Our detrital zircon U-Pb ages have a limited range, with a main population peak at 2942 Ma (65% of filtered analyses), indicating that the detritus was likely derived from a catchment with limited bedrock-age variability – a feature that is typical of small and poorly integrated watersheds with proximal sources. This depositional interpretation is consistent with a first-stage erosion cycle whereby a newly exposed (micro-)continent, with thickened crust, sheds predominantly local sediment along its fringing shelves (Reimink et al. 2021).

# 4.2 Oxidizing diamond-forming fluids and the subduction of Mesoarchean crust

Three recovered microdiamonds have  $^{13}$ C-enriched carbon isotope compositions, with  $\delta^{13}$ C values of -3.5 to -0.3 % that fall within the highest  $82^{nd}$ – $98^{th}$  percentile of carbon isotopes compared to younger Slave microdiamonds (Figure 4a) and are even more anomalous ( $88^{th}$ - $100^{th}$  percentile) compared to a database of peridotitic lithospheric diamonds globally (Stachel et al. in press). Importantly, these  $\delta^{13}$ C values and a positive average  $\delta^{15}$ N value of +3.7 ± 0.2 % (2SE; Supplementary Table S3) for nitrogen-bearing

diamond TR18-02d2 are significantly higher than the  $\delta^{13}$ C and  $\delta^{15}$ N values of Archean diamonds recovered from a gold-bearing quartz pebble conglomerate deposit in the Witwatersrand Basin of South Africa (Smart et al. 2016). In combination, the elevated  $\delta^{13}C$  and  $\delta^{15}N$  values provide strong evidence that crustal marine carbonate was present in the source. The crustal carbonate must have been brought to depths of >170 km. possibly through local subduction processes or perhaps supplied via ancient mobile lid tectonic regimes (Capitanio et al. 2020) that have been hypothesized for the ancient Slave craton (Bauer et al. 2020). Further support for the presence of carbonate species in the parental diamond fluids comes from the core-to-rim [N]-δ<sup>13</sup>C zonation trend in diamond TR18-02d2 (Figure 4b). With continuous diamond precipitation from a single fluid undergoing a Rayleigh distillation fractionation process, the model diamond N contents decrease and  $\delta^{13}$ C values increase when precipitating from an oxidized fluid or a mixed CO<sub>2</sub>/CO<sub>3</sub><sup>2</sup>-CH<sub>4</sub> fluid. CO<sub>2</sub> and carbonate are oxidized carbon species (and convert to diamond at fO<sub>2</sub> conditions of ΔFMQ -1.0 to -3.3; Stagno and Fei, 2020). The core-to-rim [N]-δ<sup>13</sup>C trend in diamond TR18-02d2 is thus strong evidence for diamond formation from an oxidizing fluid (see caption to Figure 4b for modelling details) derived from recycled crustal carbonate. In addition, Mesoarchean-aged diamonds extracted from Cenozoic kimberlites in the Slave craton contain radiogenic Os that has been interpreted to indicate the involvement of recycled material in the development of Mesoarchean lithospheric root in the nearby central Slave craton (~350 km to the SSE from the Tree River; Westerlund et al. 2006).

#### 4.3 Cold geotherm in Mesoarchean cratonic lithosphere

The temperature-pressure at the time of diamond growth can be constrained from nitrogen aggregation thermometry and elastic geobarometry of inclusion/diamond systems (Angel et al. 2017). Nitrogen is found at trace concentrations in diamond and its bonding state changes over time via diffusive processes. Nitrogen initially occurs as single atoms (C-centers), which aggregate to pairs (A-centers) and finally to four atoms surrounding a vacancy (B-centers). As this aggregation is diffusively controlled, it depends on the integrated time-temperature history as well as initial nitrogen concentration (Taylor et al. 1996). Two of the Tree River diamonds investigated in this work have no appreciable nitrogen (<10 at. ppm) but one diamond, TR-18-02-d2, contains 170–1770 at. ppm determined by SIMS spot analyses (Supplementary Figure S3). Based on the nitrogen concentration measured by FTIR (1311 at. ppm) and the associated estimate of aggregation state (4% of nitrogen in B-centers; Supplementary Table S4), an estimate of the mantle residence temperature can be provided by assuming a mantle residence time. The oldest diamonds in the Slave craton lithosphere are dated at 3.3–3.5 Ga (Aulbach et al. 2004; Westerlund et al. 2006), and our U-Pb analyses show that the Tree River detrital diamonds are older than at least 2.83 Ga. This consideration gives an upper estimate on mantle residence time of 0.65 Gyr. If we make the very conservative assumption that the Tree River diamonds resided in the mantle for anywhere between 10 Myr and 1 Gyr, mantle residence temperatures are tightly constrained at 1059–1168 °C. Such tight temperature windows are comparable to uncertainties in conventional mineral geothermometry.

The pressure of diamond formation is more difficult to estimate. The mantle pressure at the time of formation of diamond-inclusion pairs can be calculated using the elastic geobarometry approach of Angel et al. (2017): with the residual pressure within a trapped inclusion and the thermoelastic properties of host and inclusion. Fortuitously, fracture-free, nitrogen-bearing diamond TR-18-02d2, with calculated residence temperature between 1059-1168 °C, contains a <20 µm olivine inclusion, identified by single-crystal X-ray diffraction.

The measured unit-cell of the olivine is:

The above cell volume of olivine, V = 289.0 ų, can only be explained if it is under a significant residual pressure ( $P_{inc}$ ). Indeed, even a pure forsterite  $Fo_{100}$  has its cell volume at 290.3 ų. Thus, a volume of 289.0 ų definitively corresponds to the volume of an olivine under pressure (as is typical of olivines still trapped within their diamond hosts; Angel et al. 2017). Using the pressure-volume equation of state of olivine (Angel et al. 2017), we provided the  $P_{inc}$  and  $P_{trap}$  (for temperatures between 1058 and 1168°C, determined by FTIR on the diamond host) for any possible olivine composition between Mg# = 90 and Mg# = 95, see Table 3.

Table 3: inclusion pressure and formation pressure for different olivine compositions.

Mg# olivine	Calculated unit-cell volume (ų) at room pressure	P <sub>inc</sub> (GPa)	P <sub>trap</sub> (GPa, at 1059 °C)	P <sub>trap</sub> (GPa, at 1168 °C)
90	292.35	1.49	5.86	6.13
91	292.17	1.41	5.73	6.01
92	291.99	1.33	5.61	5.89
93	291.81	1.25	5.49	5.77
94	291.63	1.17	5.36	5.65
95	291.45	1.09	5.24	5.53

The vast majority of olivine inclusions released from diamonds have Mg# between > 90 and < 95.5, with the main peak at 91-93 for Iherzolitic and 92-94 for harzburgitic olivines (Stachel 2021). In a review of the Slave Craton, all peridotitic lithologies in the diamond stability field have Mg# compositions of 89.6-92.3 (Helmstaedt 2009). Given that 43% of olivine inclusions in diamonds globally lie between Fo92 and Fo93 (Stachel 2021) and no Mg# higher than 92.3 has been found beneath the Slave craton, then we view the most realistic estimate of trapping pressure to be 5.5 to 5.9 GPa (92-93 Mg#), resulting in an average and propagated uncertainty of 5.7 +/- 0.5 GPa. Based on the specific Slave craton compositions, with a lower Mg# boundary (of ~90) the pressure uncertainty may potentially be extended to 6.13 GPa (highlighted as a light-coloured box in Figure 5).

The data presented here from Mesoarchean detrital diamonds provides unambiguous evidence for the existence of a diamond-bearing lithospheric mantle root beneath the northern Slave craton prior to 2.9 Ga. Further, the pressure-temperature constraints imply

derivation of diamonds from lithosphere with a remarkably cool Mesoarchean model cratonic geotherm of 36–38 mW/m² (see Figure 5a; with extended uncertainty to 35 mW/m²; based on the Hasterok and Chapman (2011) geotherm reference model), similar to the coolest geotherms found beneath cratons today, and indicating a lithospheric base between ~210 and 240 km. This lithospheric thickness estimate from the northern portion of the Slave craton is within error of the thickness estimated using mantle xenoliths/xenocrysts (Griffin et al. 1999) for the central Slave craton (Figure 5a) at the time of kimberlite sampling (~0.055 Ga). This shows that some early deep cratonic roots were able to attain cool geotherms by the Mesoarchean.

#### 4.4 Formation and Preservation of Archean Cratonic Nuclei

Our documentation of very cool lithosphere during the Mesoarchean conservatively shows the existence of at least small blocks of "proto-cratons" by the Mesoarchean (>2.83 Ga), even if their lithospheres may not have been thermally equilibrated by then. This agrees with the suggestion of Helmstaedt (2009) that thick lithosphere must have existed beneath some parts of the Slave craton in the Meso to Paleoarchean. While a variety of tectonic models may have played a role in lithosphere formation for early cratons (Van Kranendonk 2011), the cool geotherm at >2.83 Ga documented in this study restricts the possibilities, with a requirement for rapid and extensive cooling and a lithospheric root that was thus both deep (>200 km) and narrow (likely sediment catchment region <300 km).

Lithospheric root formation through 'hot' initial state models of i) secular mantle cooling (Michaut and Jaupart 2007), ii) cooling of a depleted, stiffened mantle after extensive melting in a rift zone (Capitanio et al. 2020), and iii) melting and plume subcretion (e.g., Griffin et al. 1999) all require extensive time to cool to cratonic geotherms (0.6-3.0 Gyr; Michaut and Jaupart 2007; Capitanio et al. 2020). These models may not be realistic in forming a relatively small, thick and cold root by the Mesoarchean (Figure 5b), although a collection of these mechanisms may have contributed to the formation of cratonic lithosphere in general (Pearson et al. 2021). Lithospheric root formation through 'cold' initial state models are varieties of tectonic shortening (Eaton and Perry 2013), be it due to lithospheric stacking during collision (Helmstaedt and Schulze 1989; Carlson et al. 2005), pure-shear type mechanisms (Jordan 1988; McKenzie and Priestley 2016; Wang et al. 2018), or lateral tectonic accretion of lithosphere through successive stacking during subduction (Michaut and Jaupart 2007; Helmstaedt and Schulze 1989).

To test how the cold lithospheric mantle in the northern Slave craton was formed in the Mesoarchean, we explore the thermal consequences of two main mechanisms proposed for the formation of the Slave lithospheric mantle (Helmstaedt 2009; Aulbach et al. 2011), namely, slab/lithospheric stacking and the vertical accretion of hot plume melting residues (Figure 6). In our models, the relaxation of the lithospheric geotherm after slab-stacking shows that, as expected, at the initial thickened state the lithosphere is cold enough to form diamonds. Even though warming ensues after this initial state, the mantle thermal state after the thickening event falls within the specific temperature window at 175 km depth based on our diamond PT constraints from 50 Myr until the end of the modelling at

2000 Myr (Figure 6a, 6c). In contrast, the hot initial state of the lithosphere in our plume model does not cool into upper bounds of the diamond formation conditions for the Tree River diamonds until >750 Myr after removal of the direct plume heat source (Figure 6b, 6c). Only after 1400 Myr does the mantle lithosphere reach the average of the most likely temperature of our diamond pressure-temperature constraint. This indicates that any plume proposed to have been responsible for generating thick lithosphere in the northern Slave craton would have to have had to been active before 3.6 Ga. Although mantle plumes may possibly have been more common in the Archean, based on a higher relative abundance of komatiites (Condie and Benn, 2006), P wave seismograms of the Slave mantle reveal a layered stratigraphy linked to subduction (Bostock 1998). Layer boundaries at 70-80 km and 120-150 km with a near-horizontal mantle stratigraphy are interpreted as formation of the proto-Slave craton through shallow subduction; a dipping structure at 170 km in the west to 230 km in the east is thought to be a later addition of underplated subducted lithosphere in the Proterozoic (Bostock 1998). Therefore, we view a plume event as less likely for formation of the lithospheric mantle for the specific case of the northern Slave craton in Archean times. Instead, slab stacking is a mechanism able to rapidly generate conditions favourable for diamond stability, in a thick cool lithosphere, and we view this as the most likely model, one that is consistent with the crustal C-N isotopic signatures of the diamonds which point to the requirement for subduction. By extrapolation, we entertain the possibility that the mechanistic solution presented here may have been widespread (although not necessarily global), as indicated by the appearance of eclogitic diamonds or eclogitic xenoliths linked to lithospheric subduction in the Kalahari, Siberian, and Man cratons by 2.9 Ga (Shirey and Richardson 2011).

Recently, Haugaard et al. (2021) documented detrital chromite derived from high-Al komatiites in the southern Slave craton. These komatiites are now found in a sedimentary cover sequence that is stratigraphically correlated to the diamond-bearing sediments from the northern Slave craton documented here. Lithosphere in the region of high-Al komatiite production must have been thin (<< 100 km) to allow sufficient mantle upwelling for the extensive melting required to produce these magmas (Arndt et al. 2008). These observations, combined with both juvenile and ancient components in the Tree River diamond-gold bearing conglomerate revealed by chondritic to sub-chondritic εNd<sub>2850</sub> values (+0.4 to -5.0), indicate the input of a variety of Nd sources into the sediment catchment, a feature that can be reconciled with the notion of craton building blocks of varied lithospheric thickness and geometry. The presence of detrital diamonds and komatiite-derived chromites – two minerals that point to very different lithospheric geotherms - in the same Mesoarchean sedimentary cover sequence implies that disparate terranes had evolved and amalgamated into a single province. Crust in this region was then eroded in, and detritus routed along, relatively small watersheds at 2.83 Ga, well before the final assembly and "cratonisation" of the Slave lithosphere at ~2.62 Ga (Figure 7). The final assembly of the Slave craton from building blocks of very different geometry and thickness is likely to have been accomplished by lateral accretion and thickening, although its long-term evolution was potentially punctuated by regional disruption, thinning, and re-healing.

#### 5. Conclusions

Diamonds recovered from a gold-bearing conglomerate that also contains detrital zircon grains with concordant U-Pb ages possibly as young as ~2.83 Ga, reveal diamond formation conditions of 5.5-5.9 GPa and 1059-1168 °C based on elastic geothermobarometry on an olivine inclusion-diamond pair. These P/T conditions indicate that a cool lithospheric geotherm of 36-38 mW/m<sup>2</sup> was present in the Mesoarchean, likely in the shape of high-aspect ratio blocks (small surface area and deep). Thermal modelling indicates that a 'cold initial state' model such as slab-stacking – to create a thick and cold lithospheric root – is most consistent with the conditions required for diamond formation in the Mesoarchean in the northern Slave craton. The presence of Mesoarchean chromite grains from komatiites in a stratigraphically correlated sediment package indicates that small cratonic building blocks with deep cool roots were juxtaposed with blocks of thinner, hotter lithosphere through lateral accretion, resulting in early cratonic basin formation. Through amalgamation and thickening of these blocks (<2.7 Ga) and thermal equilibration, the more extensive, relatively uniform, thick and stable cratonic lithosphere represented by the Slave cratonic nucleus formed. We thus conclude that diamondbearing Archean sediments may document a hitherto undocumented and common scenario of Neoarchean lithospheric cratonisation from older (Paleo- to Mesoarchean) heterogeneous building blocks. Finally, the increasing discovery of diamonds in Mesoand Neoarchean sedimentary rocks implies that rapidly ascending magmas with diamond-carrying capabilities similar to kimberlites and lamproites, existed in the early Earth and were capable of sampling diamonds from the thickest lithospheric mantle. Our results from the Slave craton therefore set the stage for new, testable hypotheses on the

geodynamic record of Archean crust elsewhere, and should spur further inspection of rare Archean detrital diamonds.

## **Acknowledgements**

This research was funded by the Metal Earth project (MERC-ME-2022-21), National Science Foundation (NSF EAR-CH-2118161), Canada Research Excellence Chairs, Silver Range Resources, GEMNorth, and the Saskatchewan Research Council. Nunavut Government is thanked for permitting fieldwork. Dave Oleson is thanked for float plane logistics and Aurora Geosciences for sampling logistics. ST acknowledges her Banting post-doctoral fellowship. Al is supported by a Discovery Grant (RGPIN-2016-5720) from the Natural Sciences and Research Council of Canada. We thank reviewers Chris Hawkesworth and Oliver Nebel for their comments and Frederic Moynier for editorial handling.

#### References

Angel, R. J., Alvaro, M., Nestola, F., & Mazzucchelli, M. L. Diamond thermoelastic properties and implications for determining the pressure of formation of diamond-inclusion systems. *Russ. Geol. Geophys.* **56(1-2)**, 211-220 (2015).

Angel R.J., Mazzucchelli M.L., Alvaro M., &Nestola F. EosFit-Pinc: A simple GUI for host-inclusion elastic thermobarometry. *Am. Min.* **102**, 1957-1960 (2017).

Arndt, N., Lesher, M., & Barnes, S. Komatiite. Cambridge university press, p 487 (2008).

Aulbach, S., Griffin, W. L., Pearson, N. J., O'Reilly, S. Y., Kivi, K., & Doyle, B. J. Mantle formation and evolution, Slave Craton: constraints from HSE abundances and Re–Os isotope systematics of sulfide inclusions in mantle xenocrysts. *Chem. Geol.* **208(1-4)**, 61-88 (2004).

- Aulbach, S., Stachel, T., Creaser, R. A., Heaman, L. M., Shirey, S. B., Muehlenbachs, K., ... & Harris, J. W. Sulphide survival and diamond genesis during formation and evolution of Archaean subcontinental lithosphere: A comparison between the Slave and Kaapvaal cratons. *Lithos* **112**, 747-757 (2009).
- Aulbach, S., Stachel, T., Heaman, L. M., Creaser, R. A., & Shirey, S. B. Formation of cratonic subcontinental lithospheric mantle and complementary komatiite from hybrid plume sources. Contributions to Mineralogy and Petrology, **161(6)**, 947-960 (2011).
- Bauer, A. M., Vervoort, J. D., & Fisher, C. M. Unraveling the complexity of zircons from the 4.0–2.9 Ga Acasta Gneiss Complex. *Geochim. Cosmochim. Acta* **283**, 85-102 (2020).
- Bostock, M. G. Mantle stratigraphy and evolution of the Slave province. *Journal of Geophysical Research: Solid Earth*, **103(B9)**, 21183-21200 (1998).
- Carlson, R. W., Pearson, D. G., & James, D. E. Physical, chemical, and chronological characteristics of continental mantle. *Rev. Geophys.* **43(1)** (2005).
- Cartigny, P., Farquhar, J., Thomassot, E., Harris, J. W., Wing, B., Masterson, A., McKeegan, K., & Stachel, T. A mantle origin for Paleoarchean peridotitic diamonds from the Panda kimberlite, Slave Craton: evidence from <sup>13</sup>C-, <sup>15</sup>N-and <sup>33, 34</sup>S-stable isotope systematics. *Lithos* **112**, 852-864 (2009).
- Capitanio, F. A., Nebel, O., & Cawood, P. A. Thermochemical lithosphere differentiation and the origin of cratonic mantle. *Nature* **588(7836)**, 89-94 (2020).
- Cawood, P. A., Hawkesworth, C. J., & Dhuime, B. The continental record and the generation of continental crust. *GSA Bulletin* **125(1-2)**, 14-32 (2013).
- Condie, K. C., & Benn, K. Archean geodynamics: similar to or different from modern geodynamics? *Geophysical Monograph-American Geophysical Union*, **164**, 47-59 (2006).
- Creighton, S., Stachel, T., Eichenberg, D., & Luth, R. W. Oxidation state of the lithospheric mantle beneath Diavik diamond mine, central Slave craton, NWT, Canada. *Contrib. Mineral. Petrol.*, **159(5)**, 645-657 (2010).
- Davies, R. M., Griffin, W. L., O'Reilly, S. Y., & Doyle, B. J. Mineral inclusions and geochemical characteristics of microdiamonds from the DO27, A154, A21, A418, DO18, DD17 and Ranch Lake kimberlites at Lac de Gras, Slave Craton, Canada. *Lithos* **77(1-4)**, 39-55 (2004).
- Day, H. W. A revised diamond-graphite transition curve. Am. Min. 97(1), 52-62 (2012).
- Eaton, D. W., & Perry, H. C. Ephemeral isopycnicity of cratonic mantle keels. *Nat. Geosci.* **6(11)**, 967-970 (2013).
- Gerya, T. Introduction to Numerical Geodynamic Modelling (second edition). Cambridge University Press, 471 pp (2019).

- Griffin, W. L., Doyle, B. J., Ryan, C. G., Pearson, N. J., O'Reilly, S. Y., Davies, R., Kivi, K., Van Achterberg, E., & Natapov, L. M. Layered mantle lithosphere in the Lac de Gras area, Slave craton: composition, structure and origin. *J. Petrol.* **40(5)**, 705-727 (1999).
- Hasterok, D., & Chapman, D. S. Heat production and geotherms for the continental lithosphere. *Earth Planet. Sci. Lett.* **307(1-2)**, 59-70 (2011).
- Haugaard, R., Waterton, P., Ootes, L., Pearson, D. G., Luo, Y., & Konhauser, K. Detrital chromites reveal Slave cratons missing komatiite. *Geology* **49** (2021).
- Helmstaedt, H., & Schulze, D. J. Southern African kimberlites and their mantle sample: implications for Archean tectonics and lithosphere evolution. In *J. Ross et al (eds), Kimberlites and related rocks, GSA Spec Publ* **14(1)**, 358-368. (1989).
- Helmstaedt, H. Crust–mantle coupling revisited: the Archean Slave craton, NWT, Canada. *Lithos* **112**, 1055-1068 (2009).
- Jackson, V. Preliminary geology of the Tree River volcanic belt (part of 86P/1,2 and 8), Slave Province, EGS 1997-14a, Indian and Northern Affairs Canada, NWT Geology Division, 1:30,000 scale map. (1997).
- Johnson, C. N., Stachel, T., Muehlenbachs, K., Stern, R. A., & Armstrong, J. P. The micro-/macro-diamond relationship: A case study from the Artemisia kimberlite (Northern Slave Craton, Canada). *Lithos* **148**, 86-97 (2012).
- Jordan, T. H. Structure and formation of the continental lithosphere. *In: M.A. Menzies and K. Cox (Editors), Oceanic and Continental Lithosphere; similarities and differences. J. Petrol., Special Lithosphere Issue* 11-37. (1988).
- Kopylova, M. G., Russell, J. K., & Cookenboo, H. Petrology of peridotite and pyroxenite xenoliths from the Jericho kimberlite: implications for the thermal state of the mantle beneath the Slave craton, northern Canada. *J. Petrol.* **40(1)**, 79-104 (1999).
- McCammon, C., & Kopylova, M. G. A redox profile of the Slave mantle and oxygen fugacity control in the cratonic mantle. *Contrib. Mineral. Petrol.* **148(1)**, 55-68 (2004).
- McKenzie, D., & Priestley, K. Speculations on the formation of cratons and cratonic basins. *Earth Planet. Sci. Lett.* **435**, 94-104 (2016).
- Melton, G. L., Stachel, T., Stern, R. A., Carlson, J., & Harris, J. W. Infrared spectral and carbon isotopic characteristics of micro-and macro-diamonds from the Panda kimberlite (Central Slave Craton, Canada). *Lithos* **177**, 110-119 (2013).
- Michaut, C., & Jaupart, C. Secular cooling and thermal structure of continental lithosphere. *Earth Planet. Sci. Lett.* **257(1-2)**, 83-96 (2007).
- Nestola, F., Pasqual, D., Smyth, J.R., Novella, D., Secco, L., Manghnani, M.H., & Dal Negro, A. New accurate elastic parameters for the forsterite-fayalite solid solution. *Am. Min.* **96**, 1742-1747 (2011).

- Pearson, D. G., et al. Deep continental roots and cratons. *Nature* **596(7871)**, 199-210 (2021).
- Raal, F.A. A study of some gold mine diamonds. Am. Min. 54, 292-296 (1962).
- Reimink, J. R., Pearson, D. G., Shirey, S. B., Carlson, R. W., & Ketchum, J. W. F. Onset of new, progressive crustal growth in the central Slave craton at 3.55 Ga. *Geochem. Perspect. Lett.* **10**, 8-13 (2019).
- Reimink, J. R., Davies, J. H., & Ielpi, A. Global zircon analysis records a gradual rise of continental crust throughout the Neoarchean. *Earth Planet. Sci. Lett.* **554**, 116654 (2021).
- Shirey, S. B., & Richardson, S. H. Start of the Wilson cycle at 3 Ga shown by diamonds from subcontinental mantle. *Science* **333(6041)**, 434-436 (2011).
- Smart, K. A., Tappe, S., Stern, R. A., Webb, S. J., & Ashwal, L. D. Early Archaean tectonics and mantle redox recorded in Witwatersrand diamonds. *Nat. Geosci.* **9(3)**, 255-259 (2016).
- Smit, K. V., Timmerman, S., Pearson, D.G., Aulbach, S., Richardson, S.H., Phillips, D., & Shirey, S.B. Geochronology of diamonds. *Rev. Mineral. Geochem.* Xxx-xxx (in press).
- Stachel, T., Banas, A., Muehlenbachs, K., Kurszlaukis, S., & Walker, E. C. Archean diamonds from Wawa (Canada): samples from deep cratonic roots predating cratonization of the Superior Province. *Contrib. Mineral. Petrol.* **151(6)**, 737 (2006).
- Stachel, T., Cartigny, P., Chacko, T., & Pearson, D.G. Carbon and nitrogen in mantle-derived diamonds. *Rev. Mineral. Geochem.* Xxx-xxx (in press).
- Stachel, T. Diamond inclusion database. *Scholars Portal Dataverse*, V1, https://doi.org/10.7939/DVN/EJUE1G, (2021).
- Stagno, V., & Fei, Y. The redox boundaries of Earth's interior. *Elements: An International Magazine of Mineralogy, Geochemistry, and Petrology,* **16(3)**, 167-172 (2020).
- R.A. Stern, M. Palot, D. Howell, T. Stachel, D.G. Pearson, P. Cartigny, A. Oh. Methods and reference materials for SIMS diamond C- and N-isotope analysis. Canadian Centre for Isotopic Microanalysis, Research Report 14–01, University of Alberta, Education and Research Archive (2014).
- Stubley, M. P. & Irwin, D. Bedrock Geology of the Slave Craton, Northwest Territories and Nunavut; Northwest Territories Geological Survey, *NWT Open File2019-01*, ESRI® and Adobe® digital files. (2019).
- Taylor, W. R., Canil, D., & Milledge, H. J. Kinetics of Ib to IaA nitrogen aggregation in diamond. *Geochim. Cosmochim. Acta* **60(23)**, 4725-4733 (1996).
- Van Kranendonk, M. J. Onset of plate tectonics. Science 333(6041), 413-414 (2011).
- Vezinet, D.G. Pearson, L.M. Heaman, C. Sarkar & R.A. Stern. Early crustal evolution of the Superior craton a U–Pb, Hf and O isotope study of zircon from the Assean Lake complex and a comparison to early crust in other cratons. *Lithos*, **368-369**, 105600 (2020).

Wang, H., van Hunen, J. & Pearson, D. G. Making Archean cratonic roots by lateral compression: A two-stage thickening and stabilization model. *Tectonophysics* **746**, 562-571 (2018).

Westerlund, K. J., Shirey, S. B., Richardson, S. H., Carlson, R. W., Gurney, J. J., & Harris, J. W. A subduction wedge origin for Paleoarchean peridotitic diamonds and harzburgites from the Panda kimberlite, Slave craton: evidence from Re–Os isotope systematics. *Contrib. Mineral. Petrol.* **152(3)**, 275-294 (2006).

## **Figures**

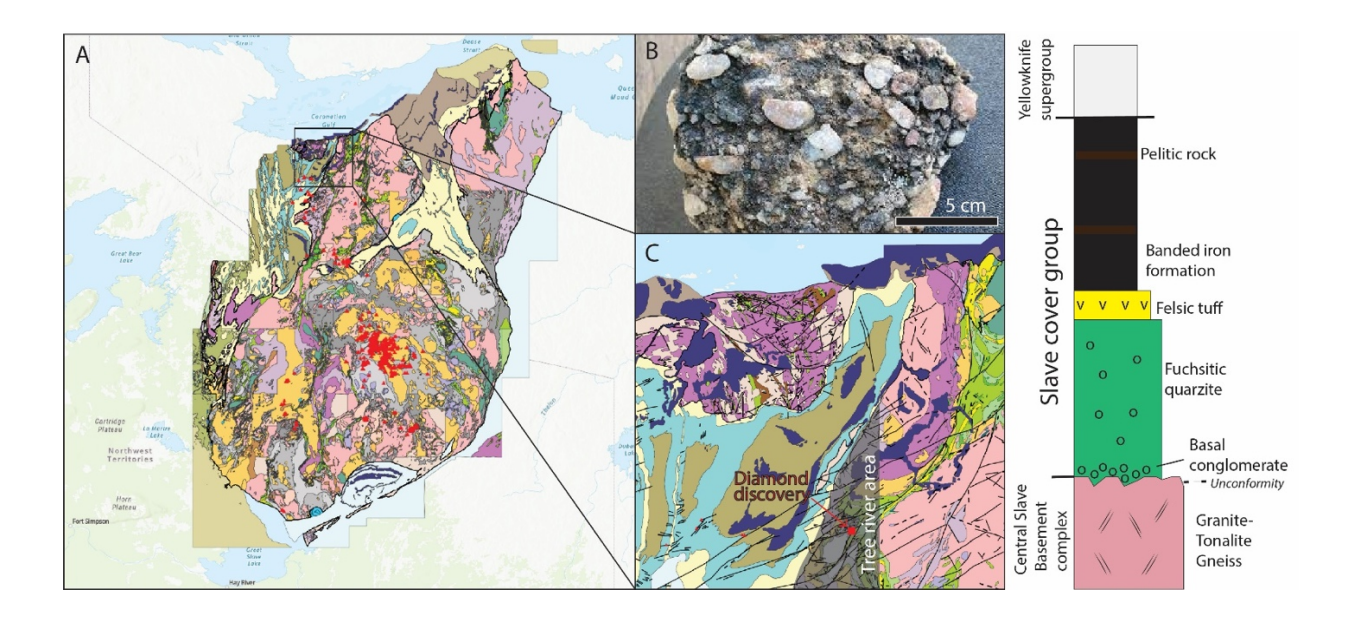


Figure 1: A) Overview of the Slave Craton from Stubley and Irwin (2019), see open file for legend of the geological units, red triangles mark kimberlite occurrences. B) Example of the conglomerate. C) Close-up geological map of the Tree river area and surroundings, modified after Stubley and Irwin (2019). The location of the sampled diamond-bearing indicated. See conglomerate is details more on https://silverrangeresources.com/projects/nunavut/tree-river/. D) Schematic stratigraphic sequence modified after Haugaard et al. (2021). The Central Slave Basement complex is 2.8-4.0 Ga, the Slave cover group is Mesoarchean in age, and the Yellowknife supergroup is <2.7 Ga. The detrital chromite (Haugaard et al. 2021), detrital zircon, diamond, gold (this study) are all from the lower unit of the Slave cover group.

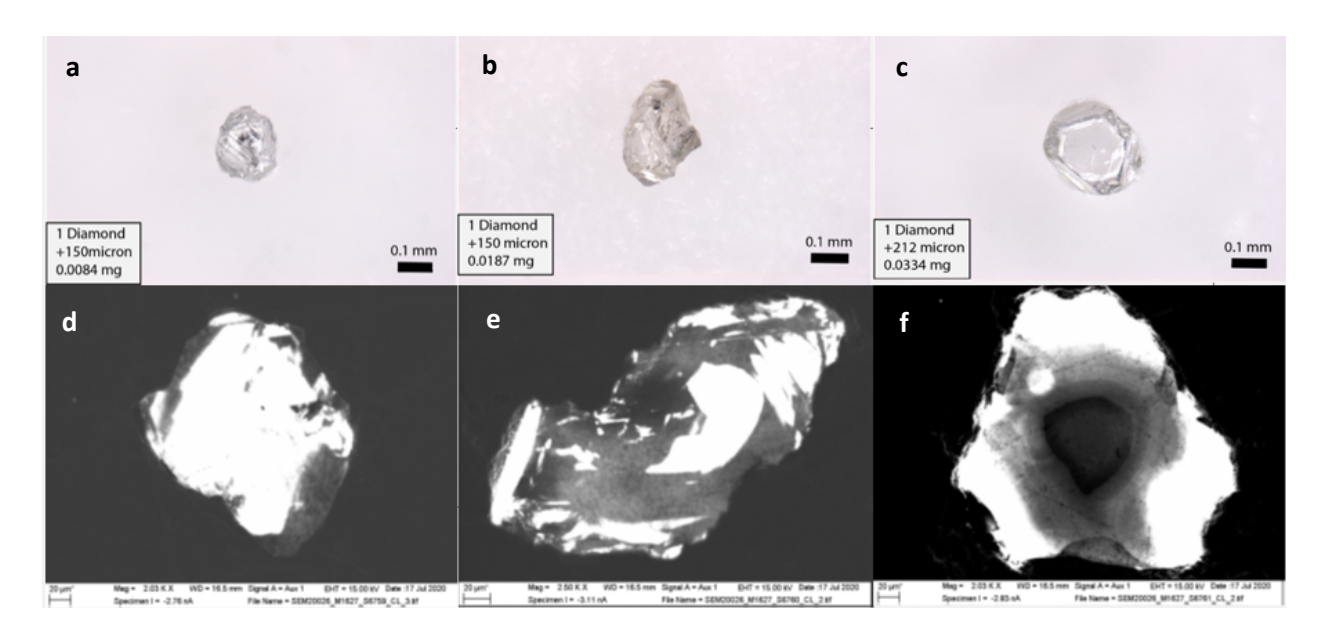


Figure 2: Reflected light images of the diamonds (a, b, c = TR-18-02c1, TR-18-02d1, TR-18-02d2) showing octahedral morphologies and cubic features at the corners (c). Cathodoluminescence images reveal the octahedral growth (d, e), and a mixed cubo-octahedral growth habit (f).

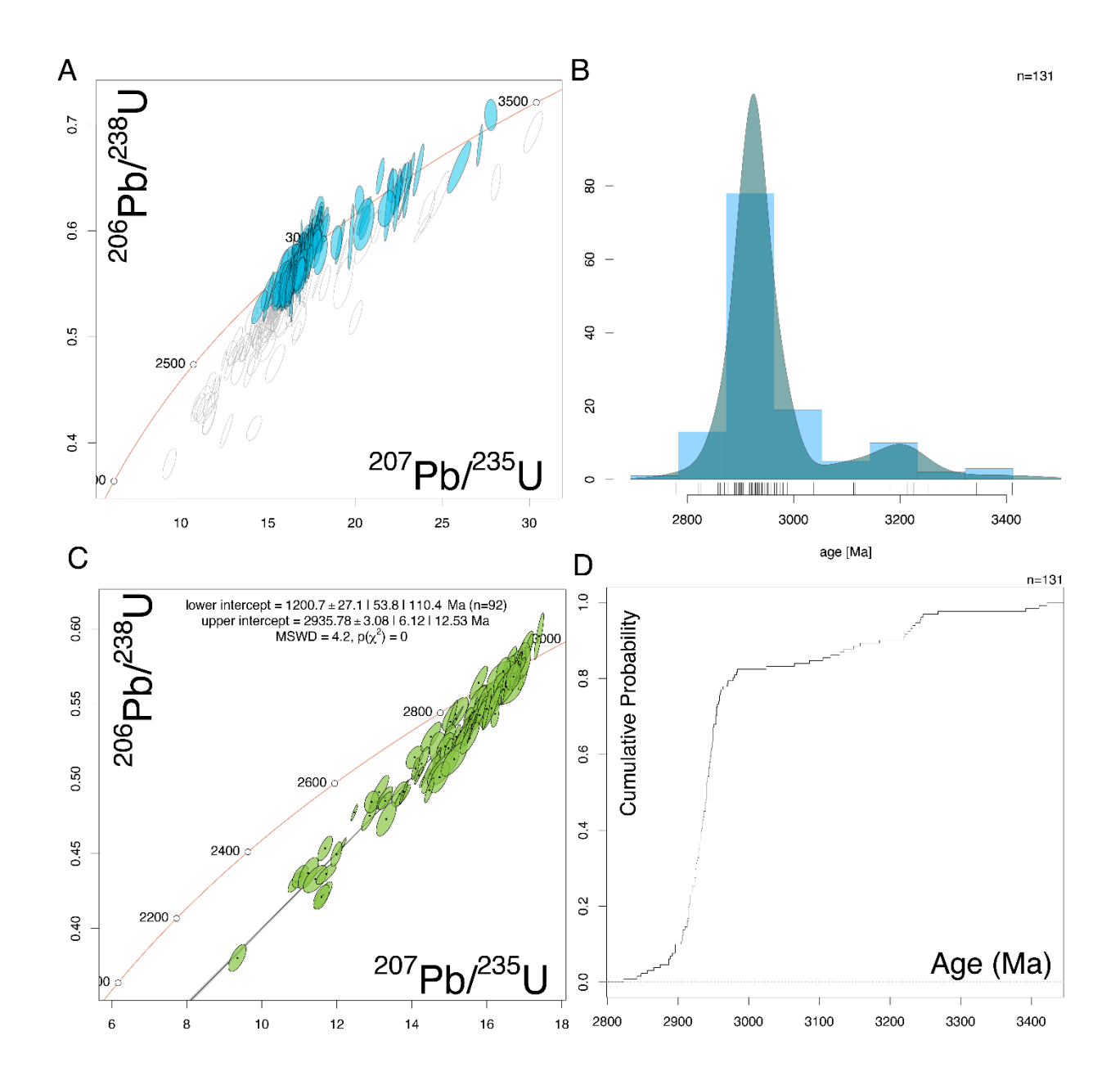


Figure 3: U-Pb ages of detrital zircons from the Tree River conglomerate and sandstone. Panel A shows the concordia plot with concordant analyses colored blue (n=131/220). Panel B shows the kernel density estimator distribution of the 131 concordant analyses, with a dominant peak at ~2.94 Ga. Panel C shows a Discordia line calculation using only the zircon, both concordant and discordant, that have the youngest <sup>207</sup>Pb/<sup>206</sup>Pb ages,

showing the probability of a Pb-loss event at ~1.2 Ga in these zircons. This argues that even the youngest concordant zircons may have experienced some ancient Pb-loss, and within the analytical precision of the LA-ICPMS technique may produce artificially young  $^{207}$ Pb/ $^{206}$ Pb ages. Panel D shows the cumulative probability of the  $^{207}$ Pb/ $^{206}$ Pb ages for all concordant analyses, again highlighting the dominance of a 2.9-3.0 Ga zircon population that represents 72% of the total analyses.

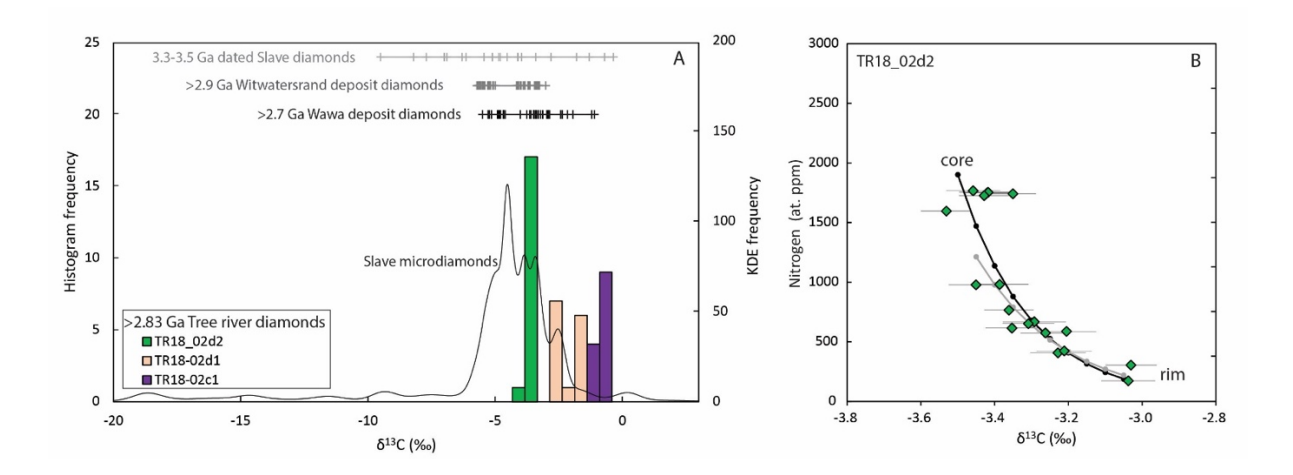


Figure 4: a) Histogram of carbon isotope compositions of the recovered microdiamonds relative to a kernel density estimation for the microdiamond population from the Slave craton (Johnson et al. 2012; Melton et al. 2013; Davies et al. 2004). Carbon isotope compositions of diamonds of comparable >2.7 Ga (Stachel et al. 2006) and >2.9 Ga (Smart et al. 2016) conglomerate deposits and dated Slave diamonds (Aulbach et al. 2009; Westerlund et al. 2006) are given. b) N- $\delta^{13}$ C was modelled for Rayleigh fractionation for core-rim growth in diamond TR18-02d2 (1SD errorbars), both from the core to rim (black line) and from the intermediate growth zone to the rim (grey line). Precipitation from an oxidizing fluid (CO<sub>2</sub>; -3.5 =  $\Delta$ diam-CO<sub>2</sub>; 12-13% precipitation from fluid; or CO<sub>3</sub><sup>2-</sup>; -1.5 =  $\Delta$ diam-CO<sub>3</sub><sup>2-</sup>; 26-28% precipitation) can explain the data. Isochemical precipitation from a water maximum fluid, with equal CH<sub>4</sub> and CO<sub>2</sub> quantities, can also reproduce the fractionation trend.

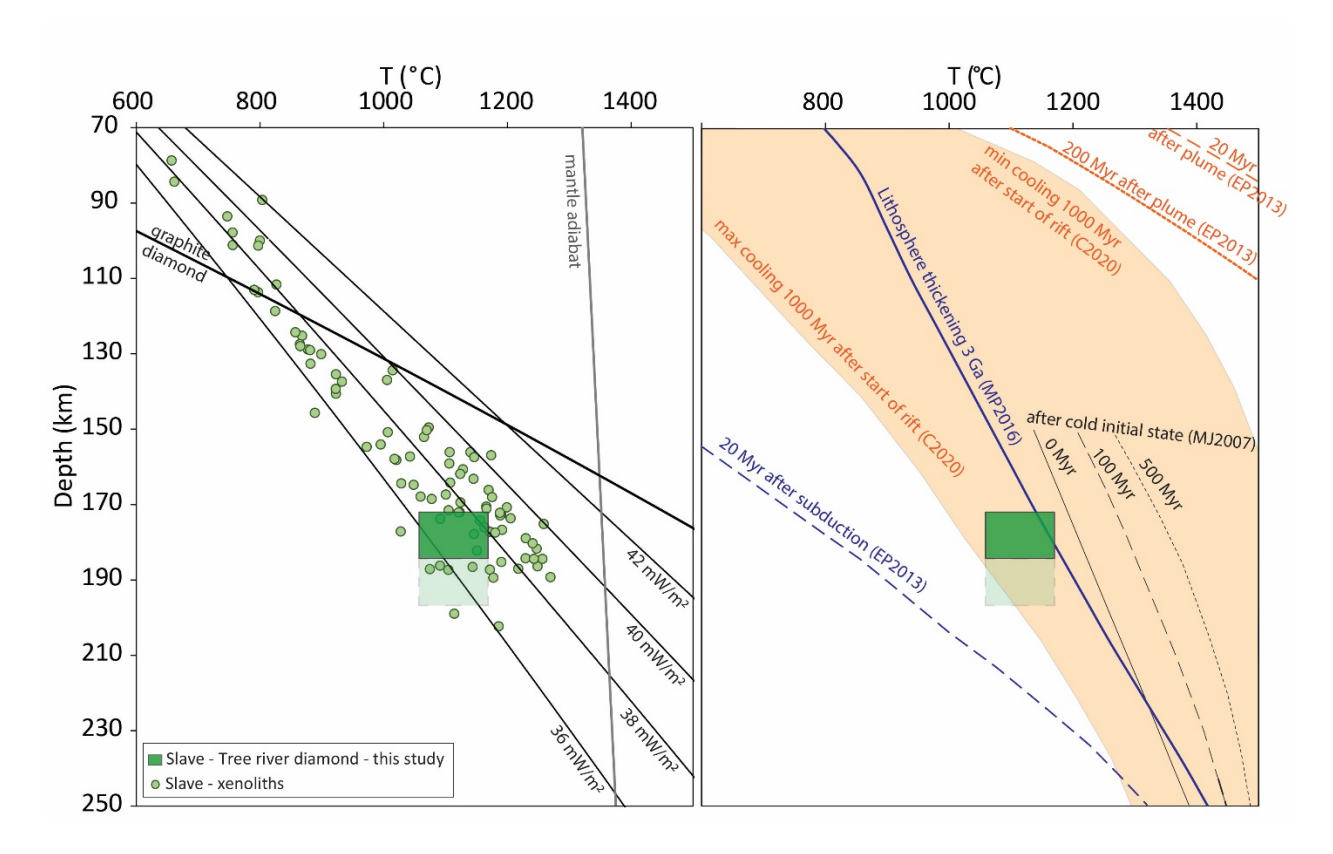


Figure 5: A) A pressure-temperature diagram showing comparable geotherms for PT constraints of the diamond at >2.83 Ga and those of xenoliths from the Slave craton at 0.05 Ga (Kopylova et al. 1999; McCammon and Kopylova 2004; Creighton et al. 2010). The graphite-diamond boundary is from Day (2012), mantle adiabat and reference geotherms from Hasterok and Chapman (2011). B) Comparison of our diamond data to different end-member lithospheric root formation models, with in black/blue geotherms for 'cold' models (subduction, lithospheric thickening; Eaton and Perry 2013; Michaut and Jaupart 2007; McKenzie and Priestley 2016) and in orange geotherms for 'hot' models (plume, rifting and melt extraction; Capitanio et al. 2020; Eaton and Perry 2013; Michaut and Jaupart 2007).

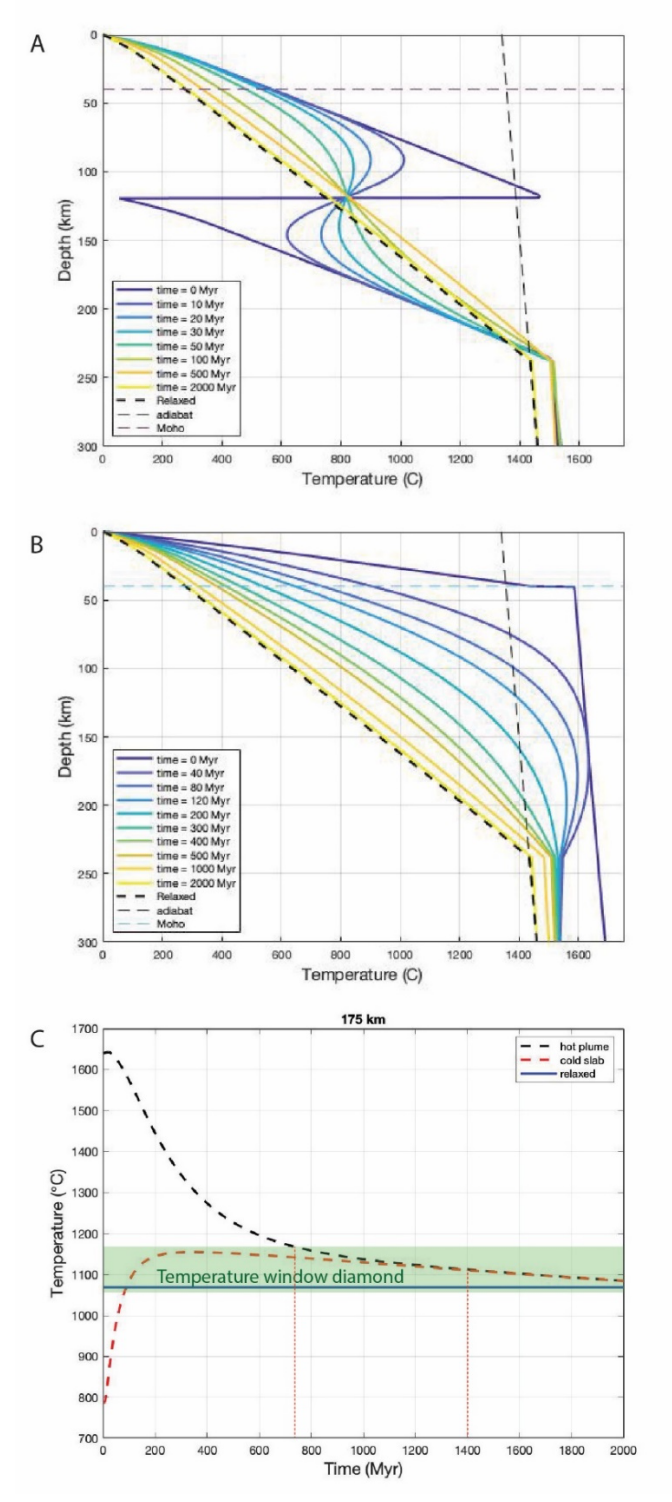


Figure 6: Thermal modelling results. Time-dependent geotherms for A) slab-stacking model and B) plume model; the mantle adiabat corresponds to the conditions after 2000 Myr, and the relaxed geotherm reflects the steady-state conditions based on the final

lithosphere properties. C) temperature evolution at 175 km depth during thermal relaxation after the modelled slab-stacking or plume event.

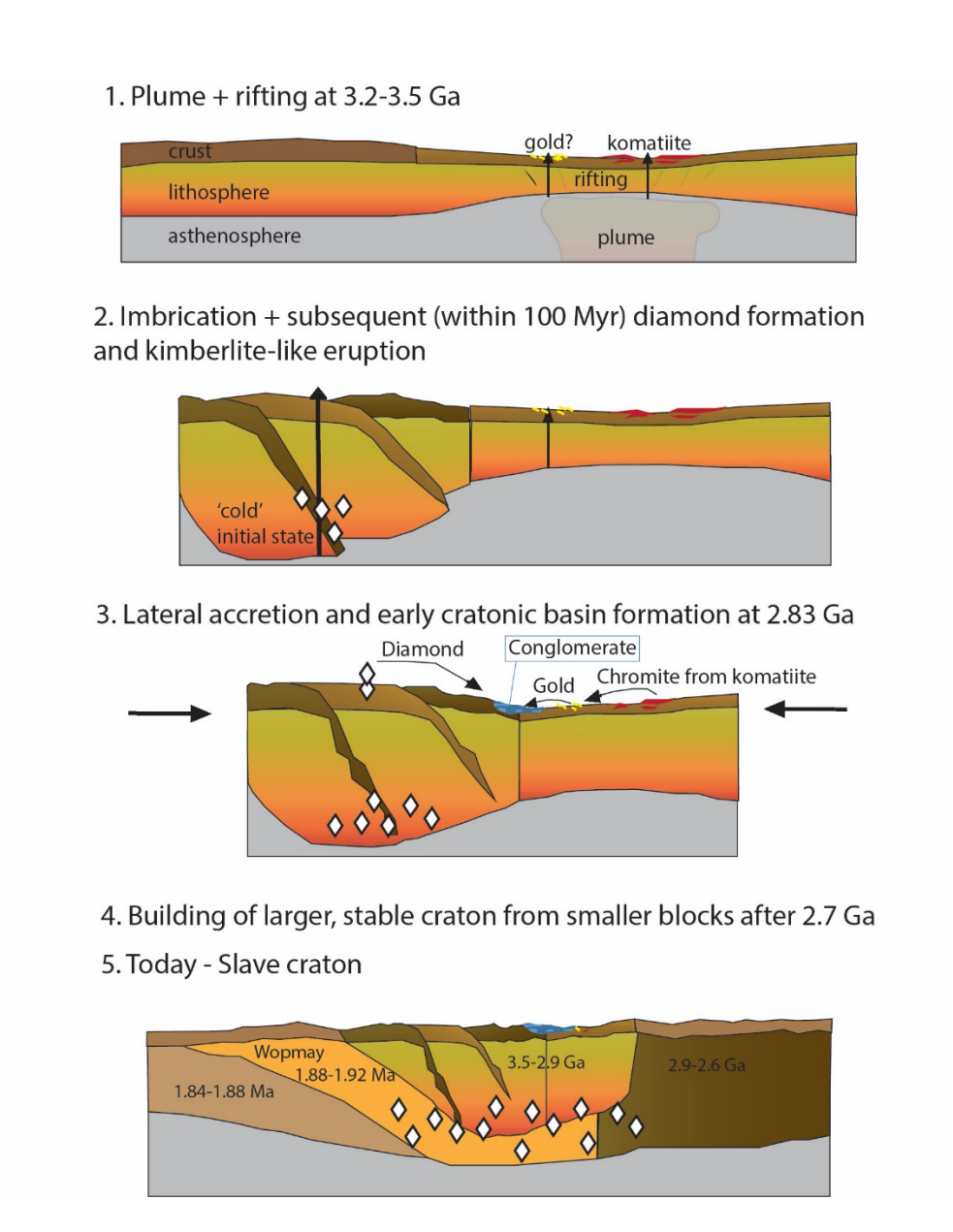


Figure 7: Schematic overview of building the lithosphere beneath the northern Slave craton between 3.5 and 2.7 Ga as constrained by data from detrital diamonds, zircons and chromite.